RESEARCH PAPER

Analysis of working face stability during obstruction removal from a box tunnel machine

Wei Liu[1] · Peixin Shi[1] · Miao Yu[1] · Pengjiao Jia[1]

Abstract

Recently, increasing numbers of box tunnels have been built in urban areas due to their high space utilization. Rectangular boring machines are commonly used in box tunneling, and tunnels are driven by thrusting prefabricated linings. Sometimes, when a tunnel machine encounters obstructions, such as boulders or steel plates, the excavation efficiency decreases. The tunnel drive has to be suspended to remove obstructions in the working chamber. Mostly, for ordinary machines, obstruction removal is carried out under open air, and the working face is no longer fully supported. This paper investigates the working face stability of box tunnels redundant on the situation in which the working face is not fully supported. According to practical experiences, the support pressure provided by the remains in the chamber is explored, and unsupported and supported areas at the face are identified. To analyze the ground stability, an analytical model is proposed by modifying the traditional silo-wedge model. In the proposed model, the wedge and prim blocks are divided into sub-blocks, and the interactions between the blocks are taken into account. Based on the proposed model, the solution of the pressure for stability is derived through limit equilibrium analysis. Parametric analysis is carried out to determine the effects of the factors on stability. A comparison of the proposed model and the traditional model is performed, and the rationality of the current model is discussed. This paper ends with the validation of the current model by investigating a case of a box tunnel in Suzhou, China.

Keywords Box tunnel · Ground stability · Limit equilibrium analysis · Silo-wedge model · Support pressure

1 Introduction

The potential of rectangular tunnels, which have high space utilization ratios, in urban underground construction has been observed. Rectangular tunnels are widely used in combined utility, roadway and subway lines. To avoid significant disturbance to the surroundings, most rectangular tunnels are built with a trenchless technique called

✉ Peixin Shi
  pxshi@suda.edu.cn

  Wei Liu
  ggoulmmeng@suda.edu.cn

  Miao Yu
  20204246014@stu.suda.edu.cn

  Pengjiao Jia
  pjjia@suda.edu.cn

1 School of Rail Transportation, Soochow University, No. 8
   Jixue Rd, Suzhou 215131, China

box jacking. Recently, many rectangular tunnels with large cross sections have been successfully installed by jacking over Chinese cities. The world's largest box tunnel with a width of 14.82 m and height of 9.45 m was recently successfully built in JiaXing, China [20]. Currently, boring machines are commonly used in tunnel box jacking to enhance the efficiency of excavation. Typically, the machine head is equipped with multiple spoke cutter heads that are driven independently. Soil cutting with multiple cutter heads causes unexpected fluctuations in support pressure, which increases the risk of face instability.

The working face stability of circular tunnels has been intensively investigated. Limit equilibrium analysis is widely used for analyzing face stability because its concept is familiar to engineers and intuitively clear. Most limit equilibrium analyses are performed based on the silo-wedge model (Horn [18]). Anagnostou and Kovári [2] used the model to investigate the working face stability of earth-pressure-balanced (EPB) shield tunnels under groundwater

seepage. In this analysis, the seepage forces applied to the wedge block were calculated using Gausses' theorem. Broere [4] modified the mode by dividing the wedge block into multiple slices to investigate slurry shield tunnel face instability in layered soils, and the slurry penetration-induced excess pore pressure on the face stability was evaluated. Anagnostou [3] developed the model by accounting for horizontal soil arching on the wedge block. Based on the model, face stability under complex conditions was explored [15, 39, 47]. The silo-wedge model was also applied to investigate the face instability of jacking tunnels [5], [19], [45].

The overburden of the soil column is important to the silo-wedge model and is intensively investigated. Nv et al. [34] employed the traditional silo-wedge model to investigate the impact of cover soil on both passive and active face failures, and the critical cover depth of a shield tunnel was identified. Chen et al. (2014) proposed a two-dimensional maximum principal stress arching model to explore the stress distribution in the soil column, and the height of failure was identified as a result. This model was verified and was in agreement with numerical simulations [8, 10, 41]. Later, Chen (9 established the concept of multi-arching that identifies the upper end-bearing arch, the middle friction, and the stability zone in the arching zone. Accordingly, a three-dimensional multi-arching model was proposed. This multi-arching model has been improved by exploring the stress-transfer mechanisms within the different arching zones [24], [44].

An upper-bound limit analysis is also employed to investigate the face instability. Constructing a kinematically admissible mechanism is the key to the upper-bound analysis. Two-dimensional mechanisms have been developed by many researchers [12, 35, 27]. Constructing a three-dimensional mechanism is more difficult. Leca and Dormieux [22] proposed a family of 3D mechanisms with conical blocks for face instability, and the model was developed for more extensive applications [28, 29, 26, 23]. The 3D mechanism construction was prompted when Mollon [30, 31, 32] applied a "point-by-point" spatial discretization technique in modeling. As a result, many kinematic models have been developed to investigate more complicated problems [16, 36, 37, 38, 40, 42]. Recently, the evolution of face failure was intensively investigated through experimental model tests (Chambon and Corte [6, 1, 20], Idinger [17], Liu [25], Chen [11], [12, 21, 22, 33]). Most of the tests observed the internal movement of soil, and the failure mechanism was revealed. The experimental tests verify the rationality of the silo-wedge model.

This paper investigates the working face stability of box tunnels, and in particular, this paper focuses on the situation in which the working face chamber exposed to free air

due to obstruction removal. Inspired by the traditional model, the modified silo-wedge model is established for this problem. In the proposed model, the wedge and prim blocks are divided into sub-blocks, and the interactions between the blocks are taken into account. Based on the proposed model, the solution of the residual support pressure is derived through limit equilibrium analysis. The verification of the current model is performed by comparison to the traditional silo-wedge model. The current model is validated by investigating a box tunnel case in Suzhou, China.

2 Problem definition

2.1 Box tunneling machines and obstructions removing

Most box tunneling machines are designed to work in earth-pressure-balanced (EPB) mode. For high excavation performance, the faces are usually designed to be equipped with multiple spoke cutter heads, and each cutter head is driven independently (Fig. 1a). Usually, double-screw conveyors are installed behind the bulkhead to expel the cuttings (Fig. 1b). When the tunnel is driven at shallow depth, the presence of unexpected obstructions, such as boulders, steel plates, and steel pipe debris, might cause excavation problems. The obstructions entering the chamber easily obstruct the cutter heads. The obstructions must be removed to ensure the performance of the cutter heads.

In project T221 of the box tunnel in Singapore, the tunnel drive was suspended several times to remove the boulders and steel debris left in the working chamber. With the man-lock retrofitted to the boring machine (Fig. 2a), the working chamber was cleared by allowing workers to enter the chamber through the man-lock under compressed air. The compressed air serves as auxiliary support for face stability. As a result, the ground surface settlement was controlled, and the working face stability was ensured.

However, for most cases, box tunnel machines are not equipped with man locks due to their high cost. The chamber clearance in these machines has to be carried out under open air, and the working face changes into open mode. In this situation, obstruction removal is riskier, and the ground becomes more vulnerable to instability. Recently, in the case of box tunnels in Suzhou, China, typical chamber obstruction removal under open air was successfully carried out. Figure 3a shows the working face configuration of the tunnel machine. The tunnel cross section has a width L of 6.9 m and height D of 4.2 m. Six independent spoke cutter heads are installed at the face for excavation, and double-screw conveyors are installed at the bulkhead. The conveyor gates have an identical diameter of
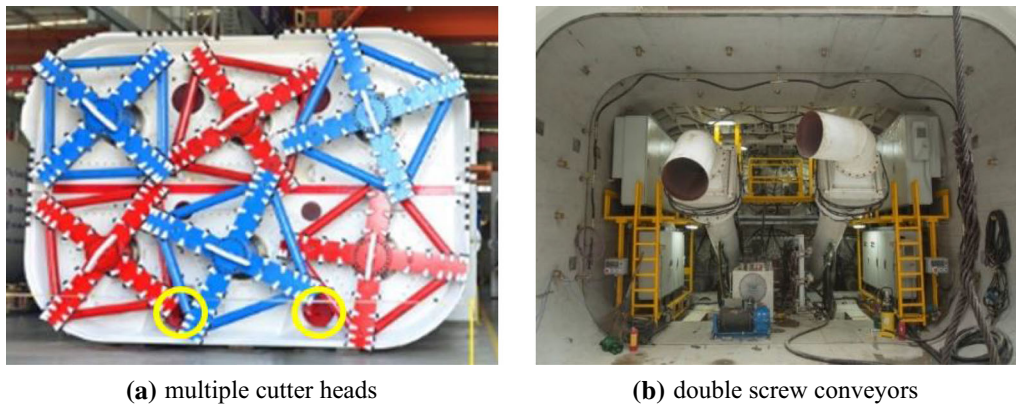
(a) multiple cutter heads

(b) double screw conveyors

Fig. 1 Typical box tunneling machine

(a) the retrofitted man lock

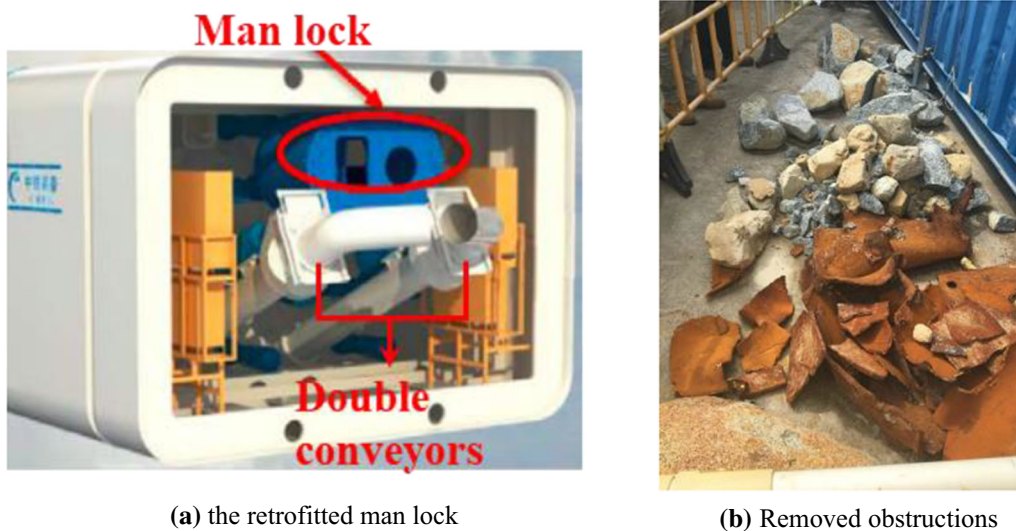**(b)** Removed obstructions

Fig. 2 Project T221 in Singapore [13]

0.56 m, and the distance between the centers of circular gates is 2.4 m. The working parameters of the cutter heads and conveyors are listed in Table 1. When the tunnel machine was driven mainly in the mixed layers of miscellaneous fills and silty clay, boulders were encountered. Some boulders that entered the chambers through the opening between the spokes obstructed the cutter heads, and the tunnel drive had to be suspended to remove the boulders. First, the double conveyors were dismantled, and the bottom gates were kept open. Then, the cuttings were removed as much as possible to identify the boulders. The boulders were manually extracted out of the chamber through the bottom gates in the end. In this case, a number of large pieces of boulders were extracted from the chamber, and the largest piece had a length over 50 cm (Fig. 3b). In the entire work, the working face stability was sustained. More details of the case are presented in Sect. 5.

2.2 Partially supported working face

Figure 4 shows the working face partially supported for the particular situation. The rectangular cross section features a normalized ratio $\lambda = D/L$. In Fig. 4a, the distribution of the remains is illustrated. Due to the configuration of the machine head, the obstructions in the chamber have to be removed from the conveyor gate at the bottom. In this work, the conveyor is dismantled while the gate is open. The cuttings are expelled through the open gate before the obstructions can be removed smoothly. The cuttings in the middle chamber are influenced most significantly during cutting expelling, and in most likely cases, the middle part of the chamber is almost empty. On the other hand, for the neighboring parts, the cuttings are influenced much less, and the remains serve as the support for the working face. During the entire work, the pressure can be measured by earth pressure sensors for the face stability assessment. In
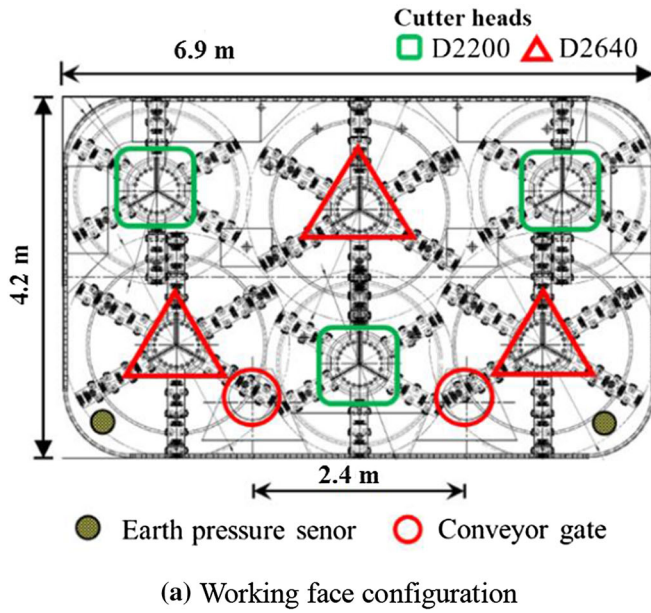
(a) Working face configuration

(b) boulder removal

Fig. 3 The box tunnel case in Suzhou, China

Table 1 Working parameters of cutter heads and conveyors

	Type	Diameter (m)	Speed (r/min)	Rated torque	Swept volume
Cutter head	D2200	2.20	0–1.54	550 kN m	–
	D2460	2.64	0–1.32	650 kN m	–
Double conveyors	D560	0.56	0–13	–	59 m³/h

Fig. 4b, the face is divided into three rectangular parts accordingly. It assumes that the middle part II with width B is completely unsupported and that the remaining Parts I and III are supported by the remaining parts in the chamber. The concept of an unsupported ratio μ defined by $\mu =$

B/L is introduced for featuring a partially supported face. The pressure applied on Parts I and III is assumed to be equal and uniform, and the pressure is denoted by s. The pressure s required for the face stability is investigated in the following section.

3 Improved model for ground stability

3.1 Profile of box tunneling

Figure 5 presents a box tunnel driven in homogenous soil. The box tunnel has a cross section with a height of D and width of L. At the face, the middle part with a width of B is unsupported, while the neighboring parts are supported by uniform pressure s. The cover depth is denoted as C and normalized by diameter D to define a dimensionless
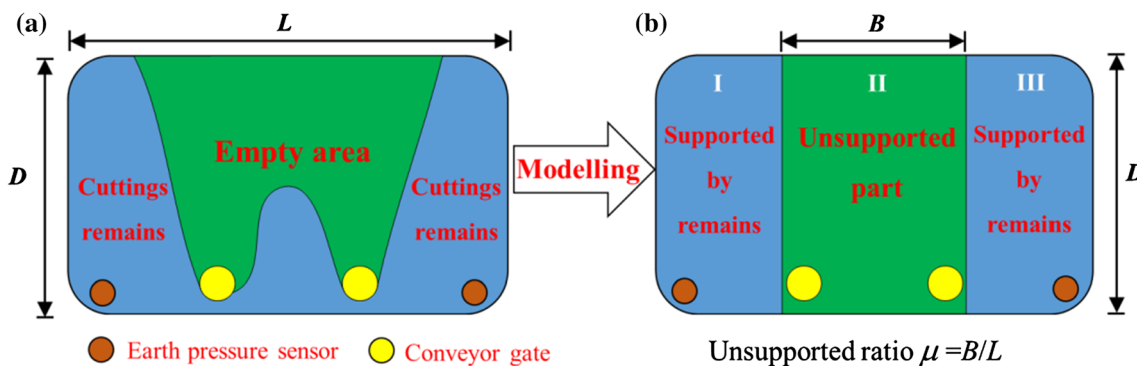

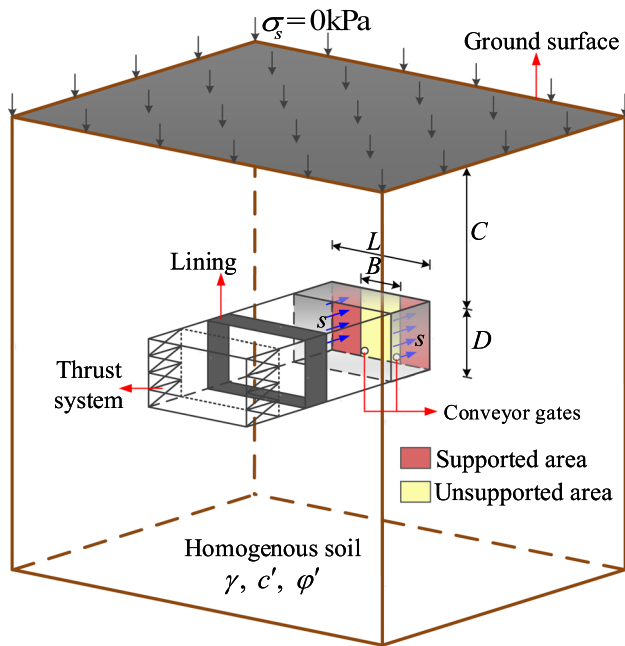**Fig. 4** Partially supported working face

Fig. 5 Profile of box tunneling

Fig. 6 The traditional silo-wedge model

parameter C/D. The surcharge on the ground surface is denoted as σ_s. In practice, when the tunnel drive is suspended for obstruction, the road traffic restrictions are suggested to be imposed. Thus, σ_s is assumed to be 0 kPa in this analysis. The soil is idealized as a rigid-plastic material obeying the Mohr–Coulomb failure condition with effective cohesion c' and effective angle of internal friction φ'. The total stress concept is adopted, and the unit weight of soil is γ.

3.2 Traditional model

Figure 6 shows the profile of the traditional silo-wedge model. The traditional model consists of a wedge block (i) and a prism block (ii). The wedge block has a height of D and width of L. This block is partially supported by the cutting remains in the chamber. On plane $abkj$, uniform pressure s is applied to the area $abod$ and $ghkj$, and the remaining part with a width of B is entirely unsupported. As shown in Fig. 6b, this wedge block is loaded by its total weight G_1, and its movement is resisted by the pressure s. The slanted plane $befk$ inclines to the horizontal at an angle of θ. At this slanted plane, there is the resultant shear force T_1 acting parallel to the slanted plane, which results from the normal force N_1, working perpendicular to the slanted plane. The side surfaces abe and fjk of the wedge are loaded by the shear forces T_2 and T_3, which are both parallel to the slant plane. The top face of the wedge is loaded by the overburden force P_1 from the soil column. In the prism block, the distribution of vertical stress along the depth in the prism can be calculated by using Broere's model [4]. In this model, the lateral earth pressure
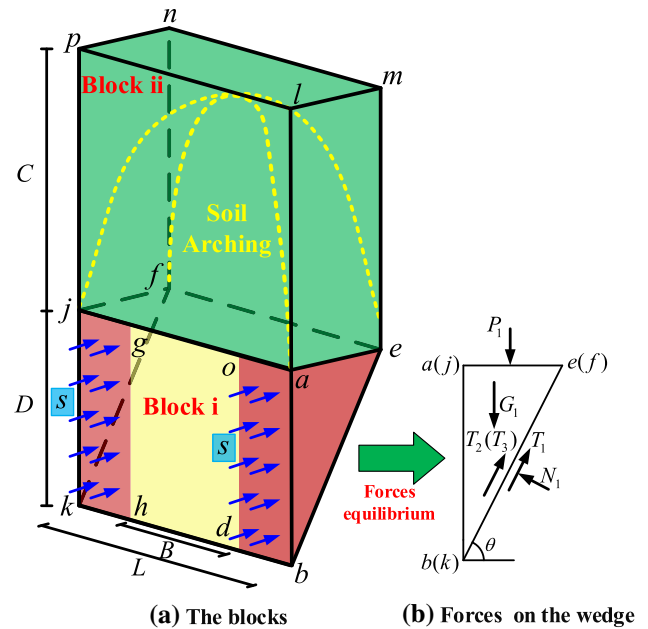
coefficient K is chosen as the at-rest lateral earth pressure coefficient K_0, and the effective length of the arching is calculated by $R_0 = LD \cot \theta / 2(L + D \cot \theta)$. Referring to previous studies [2, 4], the pressure s can be obtained based on the force equilibrium of the wedge.

By introducing the notations

$$\kappa = \frac{1 - e^{-K_0 \tan \varphi' \frac{C}{R_0}}}{K_0 \tan \varphi'} \tag{1}$$

$$\xi^- = \cos \theta (\sin \theta - \cos \theta \tan \varphi'), \tag{2}$$

and

$$\xi^+ = \sin \theta (\cos \theta + \sin \theta \tan \varphi') \tag{3}$$

the solution of pressure s can be written in the form of:

$$s = \gamma D N_\gamma^0 - c' N_c^0, \tag{4}$$

where

$$N_\gamma^0 = \frac{1}{(1 - \mu)\xi^+}$$
$$\left[\frac{2\kappa R_0/D + 1}{2} \xi^- - \frac{K_0(2\kappa R_0/L + \lambda)}{3} \cos \theta \tan \varphi' \right] \tag{5}$$

$$N_c^0 = \frac{1}{(1 - \mu)\xi^+} \left[\kappa \xi^- + 1 + \lambda \cos \theta \left(1 - \frac{2}{3} K_0 \kappa \tan \varphi' \right) \right] \tag{6}$$

3.3 Modified model

Figure 7 shows the profile of the proposed model. This model is established by modifying the traditional silo-
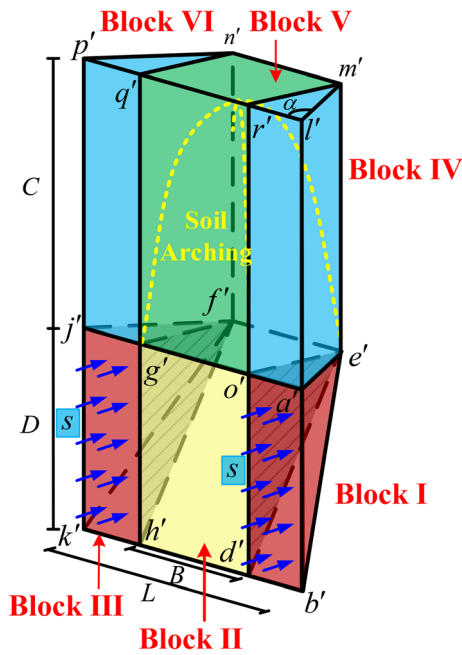
Fig. 7 The modified model

wedge model. A trapezoidal prism is used for silo modeling. The bottom corner at the top trapezoidal surface $l'm'n'p'$ is denoted by α, which is calculated by

$$\alpha = \arctan \frac{2D \cot \theta}{L - B}. \tag{7}$$

The slanted surface $b'e'f'k'$ inclines to the horizontal at an angle of θ. The modification is performed by dividing the wedge and prism blocks into three sub-blocks. The wedge block is a composite of three rigid blocks (blocks I, II and III), while the above prism block is a composite of three rigid blocks (blocks IV, V and VI). Blocks I and III are supported by pressure s subjected to the remains in the chamber, and the two are assumed to be stationary. Block II amid blocks I and III is unsupported, and its movement is inhibited by the neighboring blocks. In the prism, blocks IV and VI immediately above blocks I and III, respectively, are assumed to be stationary. Block V lies on the top surface of block II, and its movement is resisted by neighboring blocks IV and VI.

As shown in Fig. 8a, block II acts upon by (a) the resultant vertical force P'_2 of the overburden from block V onto the top surface $o'e'f'g'$; (b) the resultant normal forces (N'_{12}, N'_{32}) and shear forces (T'_{12}, T'_{32}) along the parallel lateral surfaces $o'd'e'$ and $g'f'h'$; (c) the resultant normal force N'_2 and shear force T'_2 along the slip surface $e'd'h'f'$; and (d) its weight G_2.

The vertical force P'_2 applied on surface $o'e'f'g'$ is calculated by:

$$P'_2 = \sigma_v BD \cot\theta, \tag{8}$$

where σ_v denotes the vertical stress. Respecting the arching effect within the silo, σ_v can be calculated by:

$$\sigma_v = \max\left\{0, \frac{R_1\gamma - c'}{K_0 \tan\varphi'}\left(1 - e^{-K_0 \tan\varphi'\frac{C}{R_1}}\right) + \sigma_s e^{-K_0 \tan\varphi'\frac{C}{R_1}}\right\}, \tag{9}$$

where K_0 is the at-rest lateral earth pressure coefficient ($K_0 = 1 - \sin\varphi'$) and R_1 is the semi-length of the effective arching. Referring to Broere's research [4], the semi-length R_1 of three-dimensional arching is calculated by:

$$R_1 = \frac{BD \cot\theta}{2(B + D \cot\theta)} \tag{10}$$

On slanted surface $e'f'h'd'$, the resultant normal force N'_2 is perpendicular to the surface, and the shear force T'_2 parallel to the surface results from N'_2. The relationship between N'_2 and T'_2 is presented as

$$T'_2 = \frac{c'BD}{\sin\theta} + N'_2 \tan\varphi'. \tag{11}$$

The self-weight G_2 of block II is

$$G_2 = \gamma V_2 = \frac{\gamma}{2} BD^2 \cot\theta \tag{12}$$

Due to the symmetry, on lateral surfaces $o'e'd'$ and $g'f'h'$, the resultant shear forces T'_{12} and T'_{32}, respectively, result from normal forces and are equal ($T'_{12} = T'_{32}$).

It is obvious that the condition of force equilibrium in the x-direction is stratified due to symmetry. The equilibrium conditions in the y and z directions lead to:

$$\begin{cases} N'_2 \sin\theta = (T'_2 + 2T'_{12})\cos\theta \\ P_2 + G_2 = (T'_2 + 2T'_{12})\sin\theta + N'_2 \cos\theta \end{cases} \tag{13}$$

As shown in Fig. 8b, c., block I is acted upon by (a) the resultant vertical force P'_1 of the overburden from block IV onto the top surface $o'a'e'$; (b) the resultant normal force N'_{21} and shear force T'_{21} along the interface $o'e'd'$; (c) the resultant normal forces N'_l and shear forces T'_l along the lateral surfaces $a'b'e'$; (d) the resultant normal force N'_1 and shear force T'_1 along the slanted slip surfaces $b'd'e'$; (c) the support force S on $o'a'b'd'$; and (d) its weight G'_1. It should be noted that the forces (N'_{12}, T'_{12}) and (N'_{21}, T'_{21}) are applied to block I and II interactions, respectively $(N'_{12} = N'_{21}, T'_{12} = T'_{21})$.

The resultant vertical force P'_1 applied on the top surface $o'a'e'$ is calculated by:

$$P_1 = \frac{\gamma(L - B)CD \cot\theta}{4}. \tag{14}$$

On slanted surface $b'd'e'$, the resultant normal force N'_1 is perpendicular to the surface, and the shear force T'_1
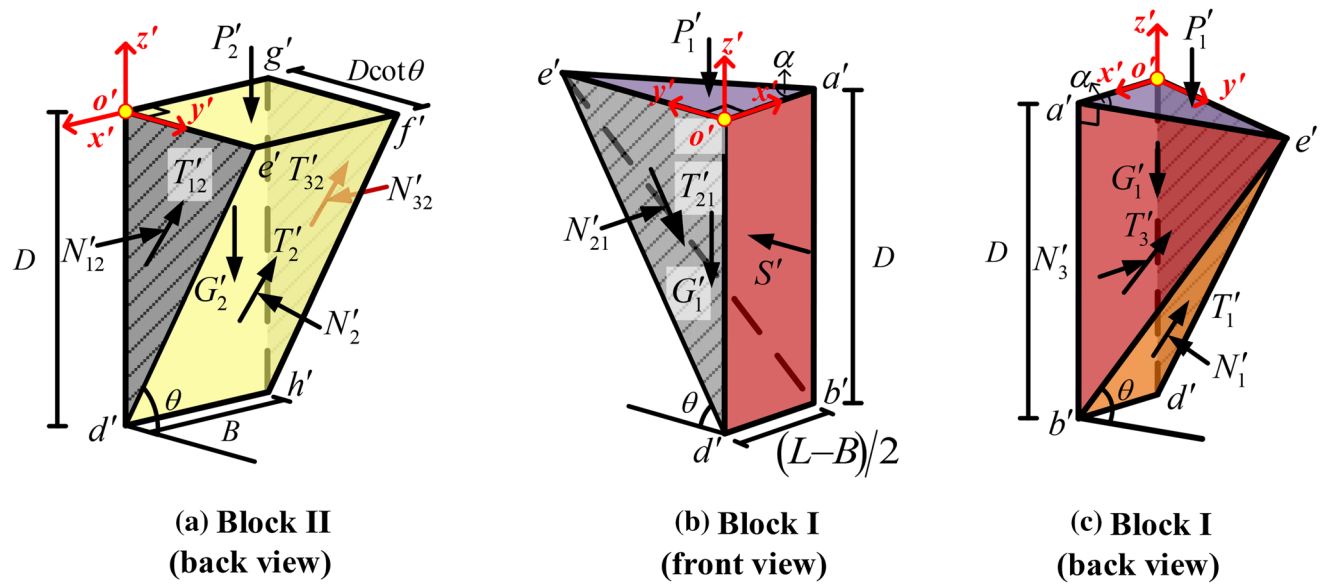
Fig. 8 The forces applied on the sub-blocks

resulting from N'_1 is assumed to be parallel to Line $d'e'$. The relationship between N'_1 and T'_1 is presented as:

$$T'_1 = \frac{c'(L-B)D}{4\sin\theta} + N'_1 \tan\varphi'. \tag{15}$$

On lateral surface $a'b'e'$, the resultant normal force N'_l perpendicular to the surface is calculated by:

$$N'_l = \frac{\cot\theta}{\sin\alpha} \int_0^D K_0 \sigma_z (D-z)\mathrm{d}z, \tag{16}$$

where σ_z is the vertical stress at a certain depth and is calculated by $\sigma_z = \gamma(C+z)$.

Resulting from N'_l, the shear force T'_l parallel to Line $b'e'$ is calculated by

$$T'_l = \frac{c'D^2 \cot\theta}{2\sin\alpha} + N'_l \tan\varphi'. \tag{17}$$

The support force S acting on plane $oabd$ is $S = s(L-B)D/2$. The weight G'_1 of Block I is

$$G'_1 = \frac{\gamma}{6}(L-B)D^2 \cot\theta. \tag{18}$$

The equilibrium conditions in the y' and z' directions lead to:

Combining equation settings (11) and (19), the pressure s is solved. After rearrangement, the pressure can be written as

$$s = \gamma D N^1_\gamma - c' N^1_c \tag{20}$$

where

$$N^1_\gamma = \left[\left(\frac{C}{2D} + \frac{1}{3}\right) + \frac{(2\kappa R_1/D+1)\mu}{2(1-\mu)}\right]\frac{\xi^-}{\xi^+} + K_0 \frac{(3C/L + \lambda)}{3(1-\mu)}$$
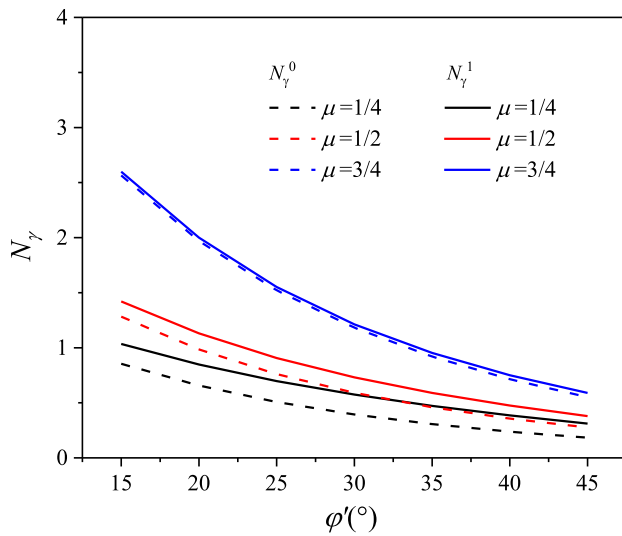$$\left(\cot\theta\cot\alpha - \frac{\cos\theta\tan\varphi'}{\xi^+}\right) \tag{21}$$

and

$$N^1_c = \frac{1}{(1-\mu)\xi^+}[\mu(\kappa\xi^- + 1) + \lambda\cos\theta] + \frac{1}{2\xi^+} \tag{22}$$
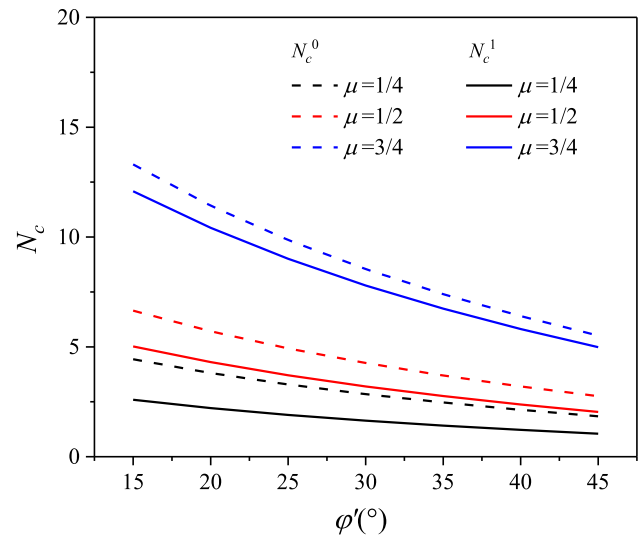
4 Stability analysis

4.1 Parametric analysis

In this part, a typical situation of $D = 6$ m and $\lambda = 0.5$ is considered. The unsupported ratio μ varies from 1/4 to 3/4. For shallowly buried tunnels, the depth ratio C/D varies
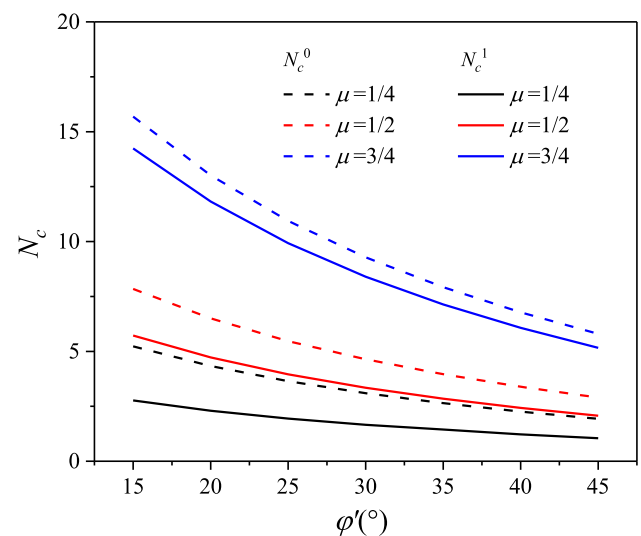
$$\begin{cases} S + T'_1 \cos\theta + T'_l \sin\alpha\cos\theta = N'_l \cos\alpha + N'_1 \sin\theta + T'_{21}\cos\theta \\ P'_1 + G'_1 + T'_{21}\sin\theta = N'_1\cos\theta + T'_l \sin\alpha\sin\theta + T'_1\sin\theta \end{cases} \tag{19}$$
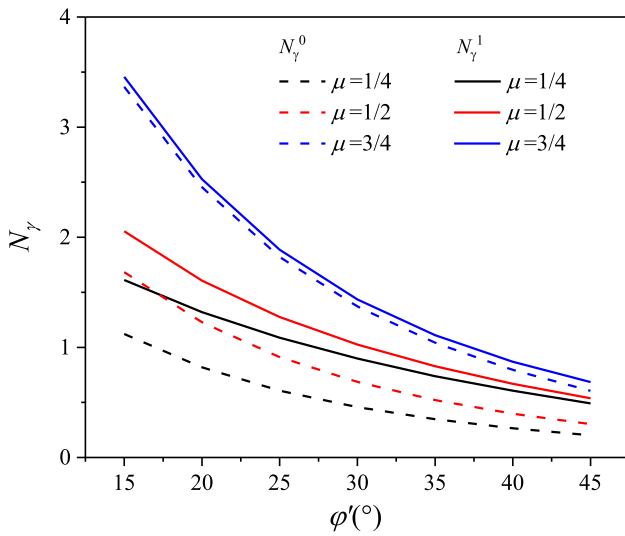
Fig. 9 Variations in N_γ^0 and N_γ^1 depending on φ'

Fig. 10 Variations in N_c^0 and N_c^1 depending on φ'

from 1 to 2, and the total stress concept is accepted for calculating the soil stress. The soil weight is chosen as $\gamma = 20$ kN/m³. The frictional angle φ' varies from 15° to 45°.

Figure 9 shows the variation of N_γ^0 and N_γ^1 depending on φ'. For $C/D = 1$ (Fig. 9a), both N_γ^0 and N_γ^1 decrease nonlinearly with increasing φ'. At constant φ', N_γ^1 is obviously higher than N_γ^0 when $\mu \leq 1/2$, and they become close to each other when $\mu = 3/4$. In Fig. (b), similar variations in N_γ^0 and N_γ^1 at $C/D = 2$ can be observed. The comparison between Figs. 9a, b shows the influence of C/D on N_γ^0 and N_γ^1. The higher C/D is, the higher are the coefficients N_γ^0 and N_γ^1. Figure 10 shows the variations in N_c^0 and N_c^1

depending on φ'. For $C/D = 1$ (Fig. 10a), both N_c^0 and N_c^1 decrease nonlinearly with increasing φ'. Both N_c^0 and N_c^1 are virtually independent of φ' when $\mu \leq 1/2$, and they become more sensitive at higher B/L. At constant φ', N_c^0 is higher than N_c^1, and the discrepancy becomes more significant at higher μ. Similar variations in N_γ^0 and N_γ^1 are illustrated in Fig. 10b.

In this part, the typical cohesion-less soil ($c'/(\gamma D) = 0$) is considered for the worse cases. As a result, Eq. (20) is simplified as $s = \gamma D N_\gamma^1$. Table 2 shows the variation in θ and α depending on φ'. It can be seen that with increasing φ', θ increases, while α decreases. The increase in θ indicates that the wedge slope becomes steeper. The decrease in α indicates the shrinkage of the base area of the prism.

Table 2 Variation in the optimal θ and α depending on φ'

φ'	$\mu = 1/4$		$\mu = 1/2$		$\mu = 3/4$	
	$\theta/°$	$\alpha/°$	$\theta/°$	$\alpha/°$	$\theta/°$	$\alpha/°$

C/D = 1

φ'	$\theta/°$	$\alpha/°$	$\theta/°$	$\alpha/°$	$\theta/°$	$\alpha/°$
20	60.4	37.2	58.0	51.3	56.1	69.6
25	63.1	34.1	60.9	48.1	59.1	67.3
30	65.6	31.2	63.6	44.8	61.9	64.9
35	67.8	28.5	66.1	41.6	64.5	62.3
40	69.9	26.0	68.4	38.4	67.0	59.5

C/D = 2

φ'	$\mu = 1/4$		$\mu = 1/2$		$\mu = 3/4$	
	$\theta/°$	$\alpha/°$	$\theta/°$	$\alpha/°$	$\theta/°$	$\alpha/°$
20	61.4	36.0	58.2	51.2	55.1	70.3
25	64.3	32.7	61.7	47.2	58.9	67.5
30	66.9	29.7	64.8	43.3	62.3	64.5
35	69.1	27.0	67.5	39.7	65.4	61.4
40	71.1	24.5	69.8	36.3	68.1	58.1

The variations in θ and α imply the volume contraction of failure blocks. Predictably, the failure zone associated with the current model decreases with increasing φ'. At constants φ' and C/D, a higher μ contributes to a lower θ but a higher α. For particular ($\varphi' = 20°$), as μ increases from 1/4 to 3/4, θ decreases from 62.5° to 59.5°, while α reversely increases from 34.7° to 67°. The decrease in θ implies that the wedge inclination approaches the slope angle of 45° + $\varphi'/2$ in the traditional model. The change in θ and α indicates that the modified model resembles the traditional model at high μ. Moreover, at constants φ' and μ, θ and α remain virtually constant with increasing C/D. The failure model is virtually independent of the ratio C/D.

4.2 Comparisons on the support pressure

Figure 11 shows the variation in normalized support pressure $s/\gamma D$ depending on frictional angle φ'. In Fig. 11a, both the current and traditional models predict that $s/\gamma D$ decreases in a similar pattern with increasing φ'. At constant φ' and μ, the current mode predicts higher $s/\gamma D$ than the traditional model does. $s/\gamma D$ associated with the current model is safer for the design. Moreover, it can be seen that the discrepancy in $s/\gamma D$ is significant at relative $\mu = 1/4$ and is reduced with increasing μ. This indicates that for scenarios with small μ, the current model is more capable of stability assessment than the traditional model. On the other hand, at high μ, the current model works similarly to the traditional model. In Fig. 11b ($C/D = 2$), a similar variation of $s/\gamma D$ depending on φ'
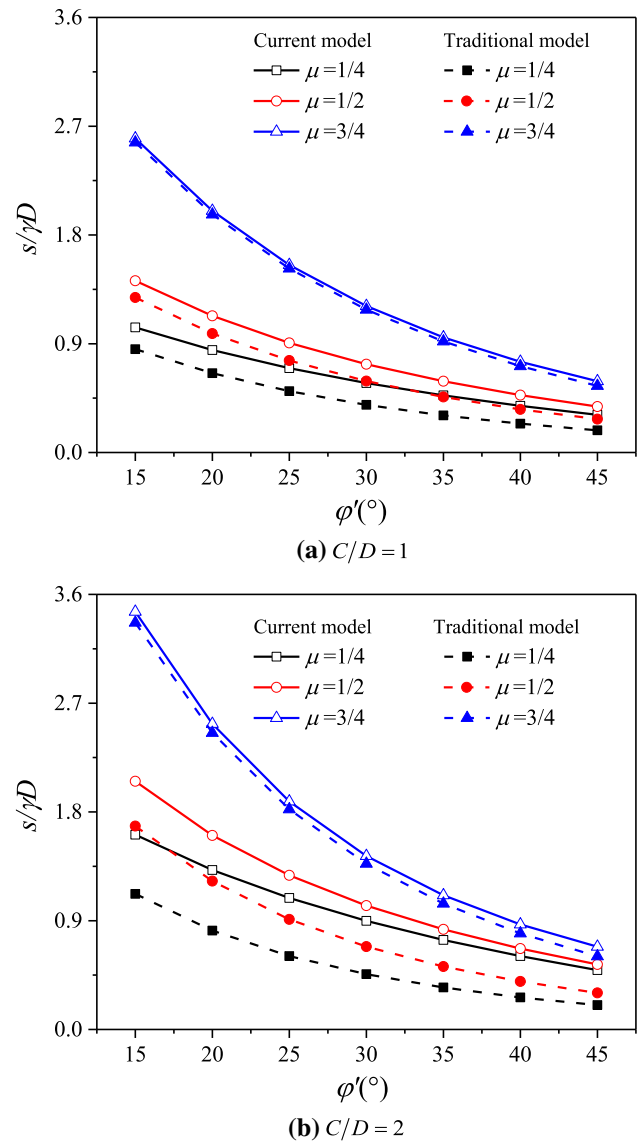

Fig. 11 Variation in $s/\gamma D$ depending on φ'

can be observed. Compared to the scenario of $C/D = 1$, both models predict higher $s/\gamma D$ at $C/D = 2$. At constant μ, the discrepancy between the models is more significant at higher C/D. The current model outperforms the traditional model for cases with either low μ or high C/D.

Figure 12 shows the variation in $s/\gamma D$ depending on μ for typical $\varphi' = 30°$. In Fig. 12a ($C/D = 1$), both models predict that $s/\gamma D$ increases with increasing μ. It can also be found that at identical L/D, the current model is less sensitive to μ than the traditional model, and the discrepancy between the models becomes less significant with increasing μ. This result probably occurs because in the current model at a relatively low μ, the resistances from the neighboring blocks on the sliding block are significant, and this effect is reduced with increasing μ. For particular, at $\mu = 0.8$, the current and traditional models predict similar
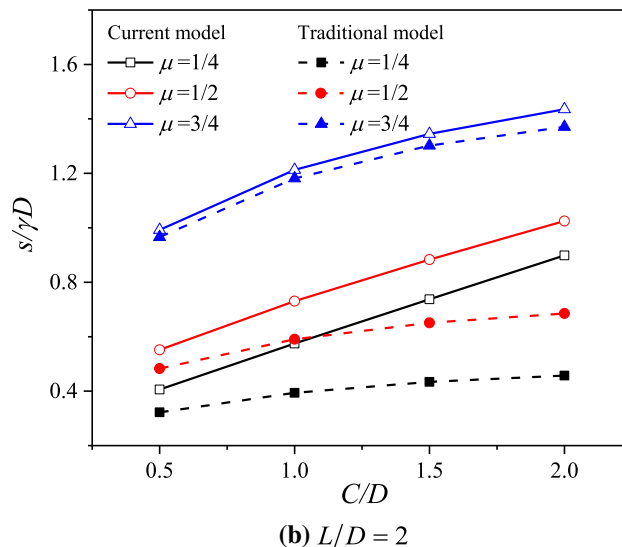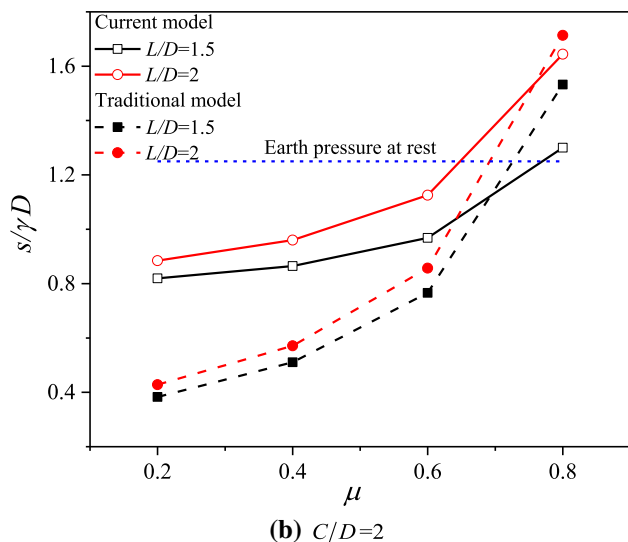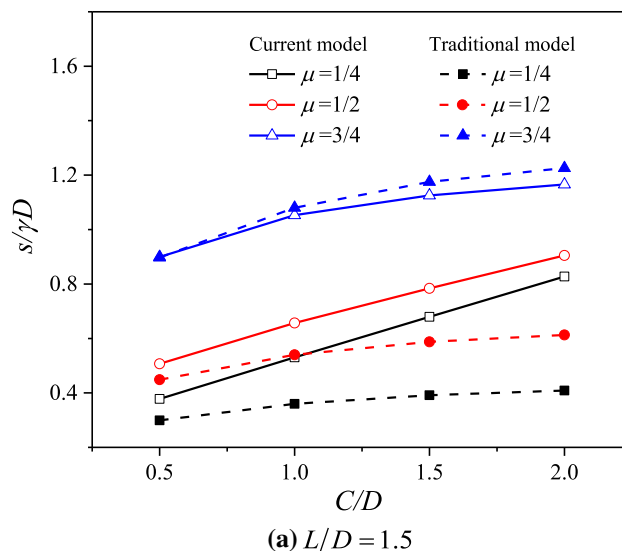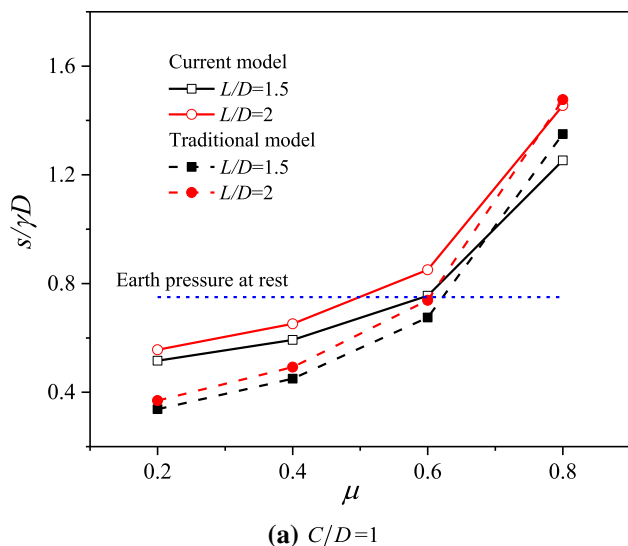
Fig. 12 Variation in $s/\gamma D$ depending on μ at typical $\varphi = 30°$

Fig. 13 Influence of C/D on $s/\gamma D$ ($\varphi' = 30°$)

results. The predicted pressure is lower than the at-rest horizontal earth pressure when $\mu \leq 0.5$. In this scenario, the current model works better than the traditional model by predicting the higher pressure, and the face stability could be assessed by comparing the measured pressure to the predicted pressure. However, when $\mu > 0.5$, the required pressures are higher than the at-rest horizontal earth pressure, which means that the cuttings should be thrusted. The above result affirms that the models are more rational when $\mu \leq 0.5$. A similar variation in $s/\gamma D$ at $C/D = 2$ is presented in Fig. 12b. The comparison shows that when μ varies from 0.2 to 0.6, the discrepancy between the models is more significant at higher C/D.

Figure 13 shows the variation of $s/\gamma D$ depending on C/D for typical $\varphi' = 30°$. It can be found that both models predict that $s/\gamma D$ increases with increasing C/D. At $\mu =$

$1/4$ and $\mu = 1/2$, the increase in $s/\gamma D$ predicted by the current model is virtually linear and rises faster than that predicted by the traditional model. The current model is more sensitive to C/D, probably because the increase in overburden on tetrahedral blocks with increasing C/D results in a higher $s/\gamma D$. At $\mu = 3/4$, the variations in $s/\gamma D$ predicted by both models are similar. This is consistent with the previous finding that both models have similar performance at a high ratio μ.

5 Case study

Figure 14 shows the profile of the mentioned box tunnel project built in Suzhou, China. This urban underground passageway tunnel is an accessory structure of a metro
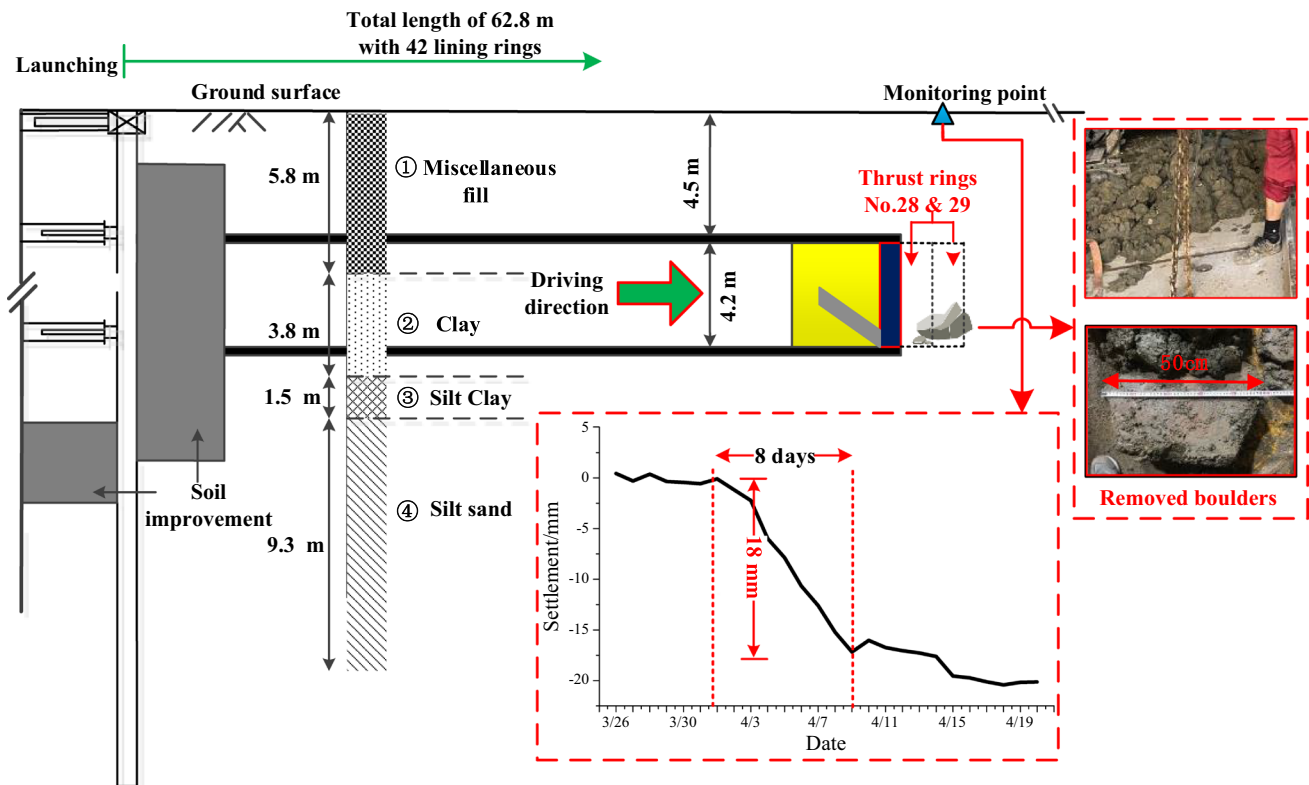
Fig. 14 Profile of the project

Table 3 Soil properties

Layer	Soil	Unit weight (kN/m³)	Young's modulus (MPa)	Cohesion c_q (kPa)	Frictional angle $\varphi_q(°)$	Osmotic coefficient k (cm/s)
①	Miscellaneous fills	18.0	4.19	–	27.0	–
②	Clay	19.0	5.44	16	26.0	3.07×10^{-6}
③	Silt clay	18.6	6.87	8	22.5	4.99×10^{-5}
④	Silty sand	19.1	10.40	1	31.0	5.37×10^{-4}

station and has a cross section with an outside width of 6.9 m and height of 4.2 m. The tunnel is approximately 62.8 m long and was built by using the jacking method. Forty-two pieces of prefabricated linings with lengths of 1.5 m and thickness of 0.45 m are used for installation. The alignments of the tunnels incline to horizontal at 2.7 ‰, and the cover depths are approximately 4.5 m. The tunnel is driven mainly in mix layers of ① miscellaneous fill and ② clay and underlain with ③ and ④. The soil properties are listed in Table 3. The groundwater table is 1 m below the ground surface. A rectangular earth-pressure-balanced boring machine is used for tunneling. The working information of the tunneling machine is presented in Sect. 2.1. The unsupported ratio approximately equals $\mu = 0.35$.

The tunnel drive was suspended for obstruction removal when lining rings No. 28 and 29 were under thrusted. The suspension of excavation lasted for approximately 8 days. During the entire work, obstruction removal was performed under open air, and the working face was not fully unsupported. In addition, no preliminary ground improvement was used because of environmental restrictions. The variation in ground surface settlement can be observed. It is clear that the ground surface settlement developed rapidly for approximately 18 mm during this work, and the rate of ground settlement was less than 3 mm/day. The accumulative settlement and the rate of settlement are both under control, and the ground stability is sustained. Then, the settlement developed more slowly when the work was finished. The subsequent settlement is attributed to soil

Table 4 Comparisons of the pressure in the chamber (kPa)

Proposed model	Traditional model	Earth pressure at rest	Measurements	
			Drive suspended	Normal drive
53.1	35.5	68.7	58–67	65–78

strength softening due to stress release and tail voids between the boring machine and the linings. Table 3 shows the comparisons of earth pressure in the chamber. In normal drilling, the earth pressure in the working chamber varies from 65 to 78 kPa. During the suspension period, the chamber is open and the support pressure s provided by the cutting remains in the chamber varies from 58 to 67 kPa. Although unexpected ground surface settlement develops, the pressure s serves to sufficiently retain the ground stability. The comparison indicates that the proposed model outperforms the traditional model and predicts higher and safer pressures. The pressure predicted by the proposed model is similar to the measured value. This comparison verifies the capability of the current model.

6 Conclusions

This paper performs an analytical investigation on the working face stability of box tunnels and, in particular, focuses on face stability during chamber obstruction removal. In this situation, the face is under open air and no longer fully supported. The face support is explored with respect to the cutting distribution in the working chamber. By modifying the traditional model, an analytical model is proposed. In the current model, the wedge block is divided into multiple blocks respecting the partially supported working face, and the interactions between the blocks are accounted for. Accordingly, the above prism block is also modified in the same way. Based on the proposed model, the solution of the support pressure is derived through limit equilibrium. The influences of factors on the face stability are discussed in parametric analysis. The comparison between the current and traditional models is carried out for verification. The results indicate that the current model outperforms the traditional model, especially when $\mu \leq 1/2$ and $s/\gamma D$ predicted by the current model are safer. The discrepancy between the models in the prediction of $s/\gamma D$ decreases with increasing μ. Finally, the current model is validated to investigate the working face stability of a box tunnel in Suzhou, China. The current and traditional models are applied for the investigation. The results predicted by the current model agree with the in situ

measurements, indicating that the current model outperforms the traditional model in this case. This research also recommends the proper distance of double conveyors with respect to $\mu \leq 1/2$ in machine design in cases of chamber obstruction removal under open air.

References

1. Ahmed M, Iskander M (2012) Evaluation of tunnel face stability by transparent soil models. Tunn Undergr Space Technol 27(1):101–110
2. Anagnostou G, Kovári K (1996) Face stability conditions with earth pressure balanced shields. Tunn Undergr Space Technol 11(2):165–173
3. Anagnostou G (2012) The contribution of horizontal arching to tunnel face stability. Geotechnik 35(1):34–44
4. Broere W (2001) Tunnel face stability & new CPT applications. Ph. D Thesis, Delft University Press
5. Broere W (2015) On the face support of microtunnelling TBMs. Tunn Undergr Space Technol 46:12–17
6. Chambon P, Corte J (1994) Shallow tunnels in cohesionless soil: stability of tunnel face. J Geotech Eng 120(7):1148–1165
7. Chen RP, Tang LJ, Yin XS, Chen YM et al (2015) An improved 3D wedge-prism model for the face stability analysis of the shield tunnel in cohesionless soils. Acta Geotech 10(5):683–692
8. Chen RP, Tang LJ, Ling DS et al (2011) Face stability analysis of shallow shield tunnels in dry sandy ground using the discrete element method. Comput Geotech 38:187–195
9. Chen RP, Lin XT, Wu HN (2019) An analytical model to predict the limit support pressure on a deep shield tunnel face. Comput Geotech 115:103174
10. Chen RP, Liu QW, Wu HN et al (2020) Effect of particle shape on the development of 2D soil arching. Comput Geotech 125:103662
11. Chen RP, Li J, Kong LG, Tang LJ (2013) Experimental study on face instability of shield tunnel in sand. Tunn Undergr Space Technol 33(1):12–21
12. Davis EH, Gunn MJ, Mair RJ, Seneviratne HN (1980) The stability of shallow tunnels and underground opening in cohesive material. Géotechnique 30(4):397–416
13. Di Prisco C, Flessati L, Frigerio G et al (2017) Experimental investigation of the time-dependent response of unreinforced and reinforced tunnel faces in cohesive soils. Acta Geotech 13:651–670
14. Foo YT (2017). Trenchless construction of pedestrian underpass using as rectangular box jack tunnel boring machine (RTBM) at Thomson-East Coast line Havelock station. Report.
15. Hörn N (1961) Horizontaler Erddruck auf senkrechte Abschlussflächen von Tunnelröhren. In: Landeskonferenz der Ungarischen Tiefbauindustrie, pp 7–16 (in German)
16. Huang MS, Li YS, Shi ZH et al (2022) Face stability analysis of shallow shield tunneling in layered ground under seepage flow. Tunn Undergr Space Technol 119:104201
17. Ibrahim E, Soubra AH, Mollon G et al (2015) Three-dimensional face stability analysis of pressurized tunnels driven in a multi-layered purely frictional medium. Tunn Undergr Space Technol 49:18–34
18. Idinger G, Aklik P, Wu W, Borja R (2011) Centrifuge model test on the face stability of shallow tunnel. Acta Geotech 6(4):105–117

19. Jancsecz S, Steiner W (1994) Face support for a large mix-shield in heterogeneous ground conditions. Tunneling' 94. Institution of Mining and Metallurgy, London, pp 531–550

20. Ji XB, Ni PP, Barla M et al (2017) Earth pressure on shield excavation face for pipe jacking considering **arching** effect. Tunn Undergr Space Technol 72:17–27

21. Kirsch A (2010) Experimental investigation of the face stability of shallow tunnels in sand. Acta Geotech 5(1):43–62

22. Lv XL, Zhou YC, Huang MS, Zeng S (2018) Experimental study of the face stability of shield tunnel in sands under seepage condition. Tunn Undergr Space Technol 74:195–205

23. Lv XL, Zeng S, Zhao YC et al (2020) Physical model tests and discrete element simulation of shield tunnel face stability in anisotropic granular media. Acta Geotech 15:3017–3026

24. Leca E, Dormieux L (1990) Upper bound and lower bound solutions for the face stability of shallow circular tunnels in frictional material. Géotechnique 40(4):581–606

25. Li PF, Chen KY, Wang F, Li Z (2019) An upper-bound analytical model of blow-out for a shallow tunnel in sand considering the partial failure within the face. Tunn Undergr Space Technol. https://doi.org/10.1016/j.tust.2019.05.019

26. Lin XT, Chen RP, Wu HN et al (2022) Calculation of earth pressure distribution on the deep circular tunnel considering stress-transfer mechanisms in different zones. Tunn Undergr Space Technol 119:104211

27. Liu W, Zhao Y, Shi P et al (2018) Face stability analysis of shield driven tunnels shallowly buried in dry sand using 1 g large-scale model tests. Acta Geotech 13(3):693–705

28. Liu W, Shi P, Chen L, Tang Q (2020) Analytical analysis of working face passive stability during shield tunneling in frictional soils. Acta Geotech 15:781–794

29. Liu W, Wu B, Shi P, Xu XY (2021) Analysis on face stability of rectangular cross-sectional shield tunneling based on an improved two-dimensional rotational mechanism. Acta Geotech 16:3725–3738

30. Michalowski RL (2001) Upper bound load estimates on square and rectangular footings. Geotechnique 51(9):787–798

31. Michalowski RL, Drescher A (2009) Three-dimensional stability of slopes and excavations. Geotechnique 59:839–850

32. Mollon G, Dias D, Soubra AH (2010) Face stability analysis of circular tunnels driven by a pressurized shield. J Geotech Geoenviron Eng 136(1):215–229

33. Mollon G, Dias D, Soubra A (2011) Rotational failure mechanisms for the face stability analysis of tunnels driven by a pressurized shield. Int J Numer Anal Method Geomech 35(12):1363–1388

34. Mollon G, Dias D, Soubra A (2013) Continuous velocity fields for collapse and blowout of a pressurized tunnel face in purely cohesive soil. Int J Numer Anal Method Geomech 37:2061–2083

35. Ma SK, Duan ZB, Huang Z et al (2022) Study on the stability of shield tunnel face in clay and clay-gravel stratum through large-scale physical model tests with transparent soil. Tunn Undergr Space Technol 119:104199

36. Nv MN, Broere W, Bosch J (2015) The impact of shallow cover on stability when tunnelling in soft soils. Tunn Undergr Space Technol 50:507–515

37. Osman AS, Mair RJ, Bolton MD (2006) On the kinematics of 2D tunnel collapse in undrained clay. Géotechnique 56:585–595

38. Pan QJ, Dias D (2016) The effect of pore water pressure on tunnel face stability. Int J Numer Anal Meth Geomech. https://doi.org/10.1002/nag.2528

39. Pan QJ, Dias D (2018) Three dimensional face stability of a tunnel in weak rock masses subjected to seepage forces. Tunn Undergr Space Technol 2018:555–566

40. Pan QJ, Dias D (2017) Safety factor assessment of a tunnel face reinforcement by horizontal dowels. Eng Struct 142:56–66

41. Perazzelli P, Leone T, Anagnostou G (2014) Tunnel face stability under seepage flow conditions. Tunn Undergr Space Technol 43:459–469

42. Senent S, Jimenez R (2015) A tunnel face failure mechanism for layered ground, considering the possibility of partial collapse. Tunn Undergr Space Technol 47:182–192

43. Rui R, van Tol F, Xia XL et al (2016) Evolution of soil arching; 2D DEM simulations. Comput Geotech 73:199–209

44. Senent S, Yi CK, Jimenez R (2020) An upper bound solution for tunnel face stability analysis considering the free span. Tunn Undergr Space Technol 103:103515

45. Tang XW, Liu W, Albers B, Savidis S (2014) Upper bound analysis of tunnel face stability in layered soils. Acta Geotech 9(4):661–671

46. Wu J, Liao SM, Liu MB, He JZ (2022) Analytical investigation on the arching effect of tunnel face in sandy ground. Tunn Undergr Space Technol 119:104207

47. Xu YJ, Liang WZ, Liu XM et al (2017) Soil mass stability at the working face of a rectangular pipe-jacking tunnel with a large section. Modern Tunnell Technol 54(5):70–77 ((**in Chinese**))

48. Zhang X, Wang MN, Wang ZL et al (2020) A limit equilibrium model for the reinforced face stability analysis of a shallow tunnel in cohesive-frictional soils. Tunn Undergr Space Technol 105:103562

49. Zingg S, Anagnostou G (2018) Effects of the hydraulic capacity of advance drainage boreholes on tunnel face stability. Tunn Undergr Space Technol 71:518–530